Front. Environ. Sci. Eng. 2022, 16(10): 131
https://doi.org/10.1007/s11783-022-1566-z

RESEARCH ARTICLE

# Highly effective visible-photocatalytic hydrogen evolution and simultaneous organic pollutant degradation over an urchin-like oxygen-doped $MoS_2/ZnIn_2S_4$ composite

**Tao Yan (✉)[1], Qianqian Yang[1], Rui Feng[1], Xiang Ren[2], Yanxia Zhao[1], Meng Sun (✉)[1], Liangguo Yan[1], Qin Wei[2]**

1 School of Water Conservancy and Environment, University of Jinan, Jinan 250022, China
2 Key Laboratory of Interfacial Reaction & Sensing Analysis in Universities of Shandong, School of Chemistry and Chemical Engineering, University of Jinan, Jinan 250022, China

## HIGHLIGHTS

- An urchin-like OMS/ZIS composite was fabricated by a facile solvothermal method.
- The OMS/ZIS exhibits superior photocatalytic $H_2$ evolution for organics degradation.
- A probable mechanism of dual-functional photocatalysis was proposed in detail.
- This work provides an inspiration for rational design of dual-functional catalysts.

## GRAPHIC ABSTRACT

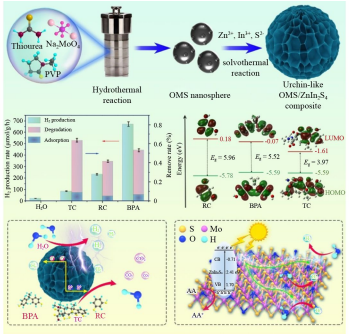


## ARTICLE INFO

*Article history:*
Received 6 November 2021
Revised 3 March 2022
Accepted 16 March 2022
Available online 15 April 2022

*Keywords:*
Dual-functional photocatalysts
Oxygen-doped $MoS_2/ZnIn_2S_4$
$H_2$ evolution
Organic pollutant

## ABSTRACT

Achieving hydrogen production and simultaneous decomposition of organic pollutants through dual-functional photocatalytic reactions has received increasing attention due to the environmentally friendly and cost-effective characteristics of this approach. In this work, an urchin-like oxygen-doped $MoS_2/ZnIn_2S_4$ (OMS/ZIS) composite was fabricated for the first time using a simple solvothermal method. The unique microstructure with abundant active sites and fast charge transfer channels further shortened the charge migration distance and compressed carrier recombination. The obtained composite exhibited an efficient $H_2$ evolution reaction rate of 12.8 mmol/g/h under visible light, which was nearly times higher than pristine $ZnIn_2S_4$, and the apparent quantum efficiency was 14.9% (420 nm). The results of the simultaneous photocatalytic $H_2$ evolution and organic pollutant decomposition test were satisfactory, resulting in decomposition efficiencies of resorcinol, tetracycline, and bisphenol A that reached 41.5%, 63.5%, and 53.0% after 4 h, respectively, and the highest $H_2$ evolution rate was 672.7 μmol/g/h for bisphenol A. Furthermore, natural organic matter (NOM) abundantly found in actual water was adopted as an electron donor for H production under simulated sunlight irradiation, indicating the promising practicability of simultaneous hydrogen evolution and NOM decomposition. Moreover, the mechanisms of the dual-purpose photocatalytic reactions, as well as the synergistic effect between the molecular structures of the organic pollutants and the corresponding adsorption behavior on the photocatalyst surface were illustrated in detail. These obtained results may serve as an inspiration for the rational design of highly efficient, dual-functional photocatalysts in the future.

© Higher Education Press 2022

## 1 Introduction

Photocatalysis is a green and sustainable technology that has received extensive attention because of its ability to utilize solar energy to address the energy crisis and

✉ Corresponding authors
E-mails: yantujn@163.com (T. Yan); smlcu@163.com (M. Sun)

environmental pollution (Yi et al., 2018). Water pollution is mainly caused by contaminants consisting of heavy-metal ions and organic pollutants (Eisenstein, 2015; Hu et al., 2017). Among these, organic pollutants possess high toxicity, carcinogenicity, and refractory degradation, posing a serious threat to human health (Zhang et al., 2019). In recent years, the photocatalytic decomposition of organic pollutants has been considered a promising water treatment technology (Liu et al., 2018c). Comparably, hydrogen production through photocatalytic water splitting has shown to be an efficient approach for transforming solar energy into hydrogen energy (Wang et al., 2018a). Nevertheless, most current research in the field of photocatalysis has either focused on the purification of wastewater or on the production of hydrogen. However, oxidative degradation and proton reduction reactions may be more valuable as photocatalytic processes for wastewater purification and energy recovery.

Dual-functional photocatalytic processes may be effective in persistently improving the efficiency of light quantum utilization, such as photocatalytic $H_2$ evolution reactions (HER) for simultaneous organic molecule degradation, which is expected to achieve $H_2$ evolution from organic wastewater. During this process, the photogenerated reactive oxygen species (ROS) decompose organics into less harmful small molecules, and photo-electrons convert hydrogen protons or water molecules into $H_2$ (Kampouri and Stylianou, 2019). Some researchers first investigated the performance of a Pt-$TiO_2$ based system for HERs using organic pollutants as electron donors (Li et al., 2001; Patsoura et al., 2006). Subsequently, numerous noble metal-based photocatalysts activated by ultraviolet light have been developed for this dual-function process (Cho et al., 2016). Jiang et al. synthesized a CdS (QDs)/g-$C_3N_4$ heterojunction activated by visible light for concurrent photocatalytic $H_2$ evolution and pollutant decomposition, which was a significant breakthrough for low-cost and visible-light responsive dual-functional photocatalysts (Jiang et al., 2018b). Since then, a variety of materials (e.g., MOFs (Kampouri et al., 2018), metal oxides (Nie et al., 2018), metal sulfides (Daskalaki et al., 2010), and carbon-based composites (Wei et al., 2019)) have been increasingly employed for dual-purpose photocatalytic technology. Amazingly, dual-functional photocatalytic performance is considered relatively unsatisfactory due to the intrinsic defects of the photocatalysts and corresponding insufficient research on the mechanism. Therefore, it is worth emphasizing that the designs and development of photocatalysts with dual-purpose activity and efficient light quantum utilization are valuable for promising practical applications.

Among the various semiconductors used for photocatalyst fabrication, metal sulfide has shown to be an extremely promising candidate for photocatalytic $H_2$ production or pollutant degradation (Chandrasekaran et al., 2019). $ZnIn_2S_4$ is a ternary chalcogenide ($AB_2X_4$) with low toxicity, a suitable band-gap (2.1–2.4 eV), and relatively high chemical stability (Chen et al., 2014; Wei et al., 2014). However, pristine $ZnIn_2S_4$ has shown limited photo-reactivity due to its higher HER overpotential and fast electron-hole recombination (Zhang et al., 2018a). In recent years, $MoS_2$ has been widely used in photocatalytic organic compound degradation and hydrogen evolution due to its many advantages such as environmental friendliness, large surface area, excellent stability, and easy preparation (Wang et al., 2018b; Gao et al., 2020). Previous studies have suggested that $MoS_2$ is a more effective $H_2$-evolution cocatalyst than many noble metals (Hou et al., 2013), due to its number of unsaturated S atom active sites on its exposed edges (Liu et al., 2015). Recently, some scholars have reported that oxygen-doped $MoS_2$ can significantly enhance photocatalytic activity and provide more surface activity reaction sites (Wu et al., 2019). Therefore, oxygen-doped $MoS_2$ may be a good choice for fabricating high-performance photocatalytic materials.

In previous studies, $MoS_2$-$ZnIn_2S_4$ composites have been mainly considered for either photocatalytic HER or organic degradation (Tian et al., 2014; Ding et al., 2015; Chai et al., 2017; Huang et al., 2017; Li et al., 2017; Guan et al., 2018; Liu et al., 2018b; Hao et al., 2019; Swain et al., 2019). Zhang et al. explored the dual-purpose photocatalytic characteristics and influencing factors of $MoS_2$ QDs@$ZnIn_2S_4$@RGO composites for the first time (Zhang et al., 2017). However, the principal issue of dual-functional systems, including thermodynamic and kinetic aspects, should be examined in more detail to further clarify the inherent mechanism of dual-functional photocatalysis. To the best of our knowledge, a systematic study on the principal issue of dual-functional systems based on $MoS_2$-$ZnIn_2S_4$ photocatalysts has not yet been reported.

In this work, we designed a novel urchin-like oxygen-doped $MoS_2$/$ZnIn_2S_4$ (OMS/ZIS) composite through the in-situ growth of $ZnIn_2S_4$ nanosheets on the surfaces of oxygen-doped $MoS_2$ (OMS) nanospheres. Then, we successfully constructed a dual-functional photocatalysis system based on the OMS/ZIS composite for simultaneous photocatalytic $H_2$ production and organic degradation. The expected dual-purpose performance was investigated using resorcinol, tetracycline, bisphenol A, and natural organic matter (NOM) as the matrix, to elucidate the mutual coupling effect of the designed photocatalytic oxidation-reduction reactions. The primary mechanism of this dual-purpose system was also discussed to clarify in detail the principal issue and internal relation. The results of this study may provide inspiration for the rational design of highly efficient, dual-functional photocatalysts in the future.

## 2 Experimental

Materials, reagents, and apparatus are shown in the Text

S1 and Text S2 of Supplementary Material.

### 2.1 Synthesis of OMS nanospheres

The OMS nanospheres were prepared according to the literature with minor modifications (Zhao et al., 2019). $Na_2MoO_4 \cdot 2H_2O$ (2 mmol/L), polyvinyl pyrrolidone (1.5 mmol/L), and thiourea (8 mmol/L) were dissolved in 40 mL deionized water. After stirring, the clear solution was transferred to a Teflon-lined stainless-steel autoclave and heated at 180 °C for 36 h. After natural cooling, the product was centrifuged and washed with deionized water, and dried in oven at 60 °C.

### 2.2 Synthesis of the OMS/ZIS composite

The OMS/ZIS composite was fabricated using a one-step solvothermal method. The as-prepared OMS nanospheres were ultrasonically dispersed in 70 mL of ethylene glycol. Next, $ZnCl_2$ (1 mmol/L), $InCl_3 \cdot 4H_2O$ (2 mmol/L), and thioacetamide (4 mmol/L) were dispersed in the solution. Then, the resultant mixture was transferred to a 100 mL Teflon-lined autoclave and maintained at 120 °C for 4 h. After cooling to room temperature, the precipitates were thoroughly rinsed with distilled water and ethanol, and then dried at 60 °C. The as-synthesized composites with different OMS mass ratios of 5%, 10%, 15%, and 20% were designated as 5-OMS/ZIS, 10-OMS/ZIS, 15-OMS/ZIS, and 20-OMS/ZIS, respectively. For comparison, pristine $ZnIn_2S_4$ was synthesized through the same process without OMS adding. A physically mixed OMS/ZIS (P10-OMS/ZIS) sample was obtained by finely grinding pristine $ZnIn_2S_4$ and OMS nanospheres. A schematic of the fabrication process is shown in Scheme 1.

### 2.3 Photocatalytic performance evaluation

All photocatalytic experiments were performed in a 100 mL pyrex glass reactor connected to a closed-cycle circulation and exhaust system (Fig. S1). A 300 W Xe lamp (CEL-SPH2N-S9, China) with a cutoff filter ($\lambda$ > 420 nm) was used as visible light source. The lamp was positioned 13 cm away from the reactor, with an average irradiated intensity of 28.7 mW/cm$^2$. Typically, 15 mg photocatalyst was dispersed in 50 mL distilled water with 0.1 mol/L ascorbic acid as a sacrificial reagent, or the same volume of 50 mg/L organic pollutants solution (resorcinol (RC), tetracycline (TC), and bisphenol A (BPA)). Before testing, the photo-reaction system was subjected to vacuum until stable pressure gauge (< −0.1 MPa), and the suspension was vigorously stirred in the dark for 30 min to establish an adsorption-desorption equilibrium.

During the test, the solution was maintained at 6 °C by a flow of cooling water. The produced $H_2$ was detected using online gas chromatography (GC7920, China Education Au-light, China; $N_2$ carrier, 5A molecular sieve column, TCD detector). The solution was drawn and centrifuged to remove the residue. The concentration of organic pollutants was measured using an ultraviolet-visible-near-infrared (UV-vis-NIR) spectrophotometer (Lambda 900, PerkinElmer, USA).

## 3 Results and discussion

### 3.1 Characterization of the synthesized materials

The X-ray diffraction (XRD) patterns of OMS, ZIS, and OMS/ZIS composite are shown in Fig. 1. For OMS, the characteristic peaks located at 12°, 33°, and 59° were assigned to the (0 0 2), (1 0 0), and (1 1 0) diffraction planes of $MoS_2$, respectively (JCPDS No. 37-1492) (Zhang et al., 2017). Notably, the low-angle shift of the (0 0 2) crystal plane implied that oxygen was successfully doped into the lattice (Zhang et al., 2018b). The pure $ZnIn_2S_4$ sample showed six main diffraction peaks, which appeared at 21.5°, 28.02°, 47.50°, and 52.80°, and were attributed to the (0 0 6), (1 0 2), (1 1 0), and (1 1 6) lattice

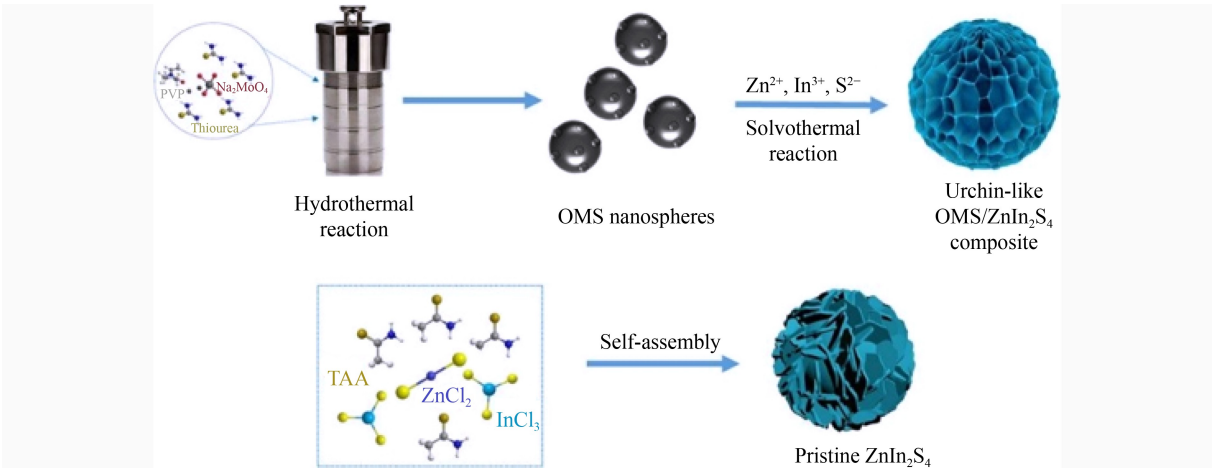


**Scheme 1** Schematic showing the fabrication process of the OMS/ZIS composite.

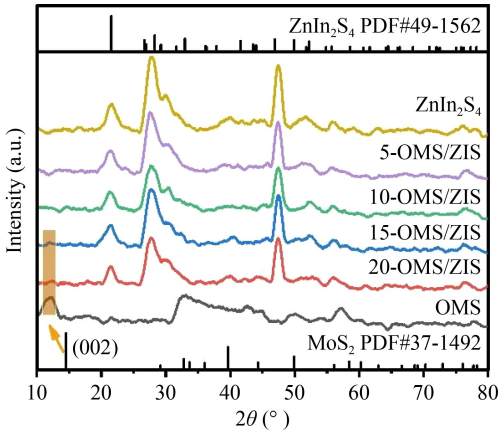


**Fig. 1** XRD patterns of OMS, $ZnIn_2S_4$, and the OMS/ZIS composites.

planes of hexagonal $ZnIn_2S_4$ (JCPDS No. 03-065-2023) (Yang et al., 2018), respectively. Of note, no diffraction peaks for OMS were observed in XRD pattern of the OMS/ZIS composite, which was attributed to the small amount of OMS content and the low diffraction intensity of OMS.

The microstructures of the synthesized urchin-like oxygen-doped $MoS_2/ZnIn_2S_4$ composite was investigated by scanning electron microscopy (SEM) and transmission electron microscopy (TEM). As shown in Figs. 2(A) and 2(B), the OMS nanosphere exhibited a wavy surface with a diameter ~350 nm (Fig. S2), and pure $ZnIn_2S_4$ presented aggregation of numerous cross-linked nanosheets. As shown in Figs. 2(C) and 2(D), the OMS/ZIS composite was composed of microspheres with dimensions in the range of 300–400 nm, which were assembled by dense flower-like nanosheets. The uniform aggregation of ultrathin $ZnIn_2S_4$ nanosheets on the surface of the OMS nanosphere formed an intimately connected heterogeneous interface. Similar observations were also made from the TEM image shown in Fig. 2(E), and the SEM and TEM images showed the urchin-like architecture of the as-prepared OMS/ZIS composite.

According to the high resolution transmission electron microscope (HRTEM) images of 10-OMS/ZIS (Fig. 2(F)), the two lattice fringes of 0.32 and 0.65 nm were assigned to the (1 0 2) and (0 0 2) planes of $ZnIn_2S_4$ and OMS (Byskov et al., 1999; Liu et al., 2018a), respectively. The tight combination of the two components facilitated the transfer and separation of the photo-induced carriers. Notably, the lattice spacing distance of 0.65 nm was

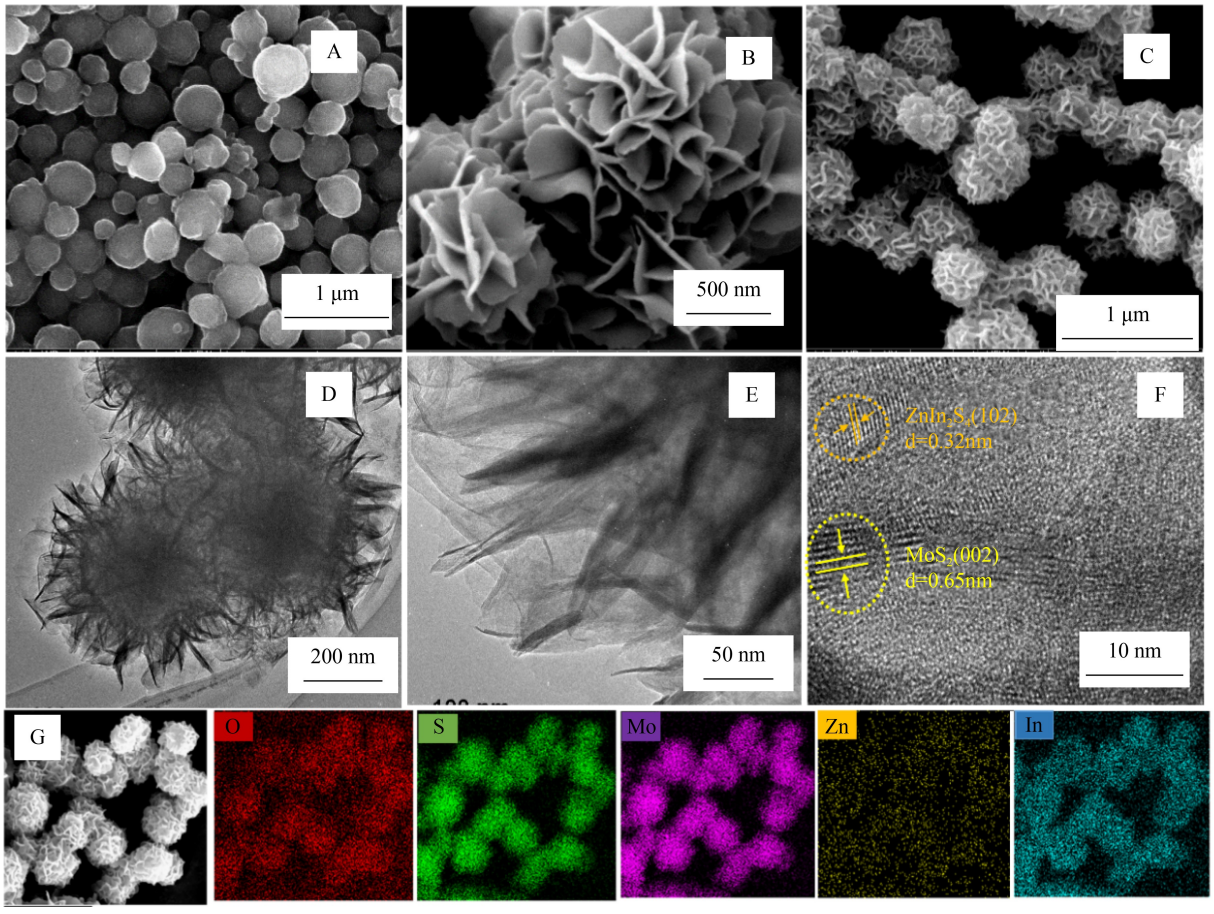


**Fig. 2** SEM images of OMS (A), $ZnIn_2S_4$ (B), and 10-OMS/ZIS (C); TEM images of 10-OMS/ZIS (D–E); HRTEM image of 10-OMS/ZIS (F); SEM image of 10-OMS/ZIS and (G) corresponding elemental mapping images.

significantly larger than characteristic $MoS_2$ (0.62 nm) due to the S sites that were replaced by the doped O in the lattice (Zhang et al., 2018b). Elemental mapping (Fig. 2 (G)) and energy dispersive spectroscopy spectra (Fig. S3) further confirmed the presence and distribution of O, S, Zn, In, and Mo elements, which strongly supported the SEM and TEM observations.

The elemental composition and chemical states of the ZIS, OMS, and 10-OMS/ZIS samples were further characterized by XPS. According to the survey spectra, Zn, In, S, Mo, O, and C elements were detected in the 10-OMS/ZIS composite (Fig. 3(A)). Furthermore, another peak at 226.6 eV was indexed to S 2s (Jo and Natarajan, 2016). Compared to the binding energies of Zn 2p (1021.1 eV and 1044.2 eV for $2p_{3/2}$ and $2p_{1/2}$) and In 3d (444.6 eV and 452.1 eV for $3d_{5/2}$ and $3d_{3/2}$) of ZIS, all peaks shifted to higher binding energies after the incorporation of ZIS and OMS (Figs. 3(B) and 3(C)), implying strong interactions between the two components and a decrease in electron density. Hence, we deduced that electrons could easily transfer from ZIS to OMS (Xu et al., 2022). As shown in Fig. 3(D), the spectra of S could be divided into two peaks, corresponding to S $2p_{3/2}$ (161.8 eV), S $2p_{1/2}$ (162.9 eV), and $S^{6+}$ (169.7 eV), which further confirmed the $S^{2-}$ chemical state (Yuan et al., 2016). For Mo, the two peaks at 228.8 eV and 231.8 eV were assigned to Mo $3d_{5/2}$ and Mo $3d_{3/2}$, respectively, confirming the $Mo^{4+}$ chemical state (Fig. 3(E)) (Zhao et al., 2019). As shown in Fig. 3(F), Mo-O was observed, which was consistent with the XRD results and further verified oxygen doping.

The optical absorption properties of the as-prepared samples were investigated by UV-Vis diffuse reflectance spectroscopy. As shown in Fig. 4(A), the absorption edge of pristine $ZnIn_2S_4$ was approximately 490 nm. However, the OMS/ZIS composite displayed a distinct increase in visible light absorption, because the coupling of black OMS effectively improved the light utilization of $ZnIn_2S_4$. Moreover, the marked red-shifts were in accordance with the higher loading of OMS, which was consistent with the color changes of the samples from light yellow to dark green (Fig. 4(A) inset). The band gaps ($E_g$) of $ZnIn_2S_4$ and the OMS/ZIS composites were obtained from the plots of $(\alpha h\nu)^2$ versus photon energy ($h\nu$). As illustrated in Fig. 4(B), the $E_g$ values of $ZnIn_2S_4$, 5-OMS/ZIS, 10-OMS/ZIS, 15-OMS/ZIS, and 20-OMS/ZIS were estimated as 2.41, 2.28, 2.16, 1.88, and 1.67 eV, respectively. Furthermore, Mott-Schottky (M-S) plots were used to characterize the conductivity types and conduction band potentials ($E_{CB}$) of the samples. As shown in Fig. S4, both $ZnIn_2S_4$ and OMS exhibited typical characteristics of n-type semiconductors due to the positive slope of the M-S plots. The $E_{CB}$ values of $ZnIn_2S_4$ and OMS were approximately −0.71 and −0.32 V (*vs.* normal hydrogen electrode, NHE), respectively. Thus, the suitable band gap and enhanced visible light absorption ability of OMS/ZIS were beneficial for improving photocatalytic activity (Zhang et al., 2018c).

The surface area and pore structure of the as-prepared composite were assessed by $N_2$ adsorption-desorption measurements (Fig. S5 and Table S1). The results showed that the urchin-like structure of OMS/ZIS effectively increased the specific surface area, suggesting more active sites for the progression of catalytic reactions. However, the specific surface area of the catalysts was not the decisive factor that affected bifunctional activity in this study.

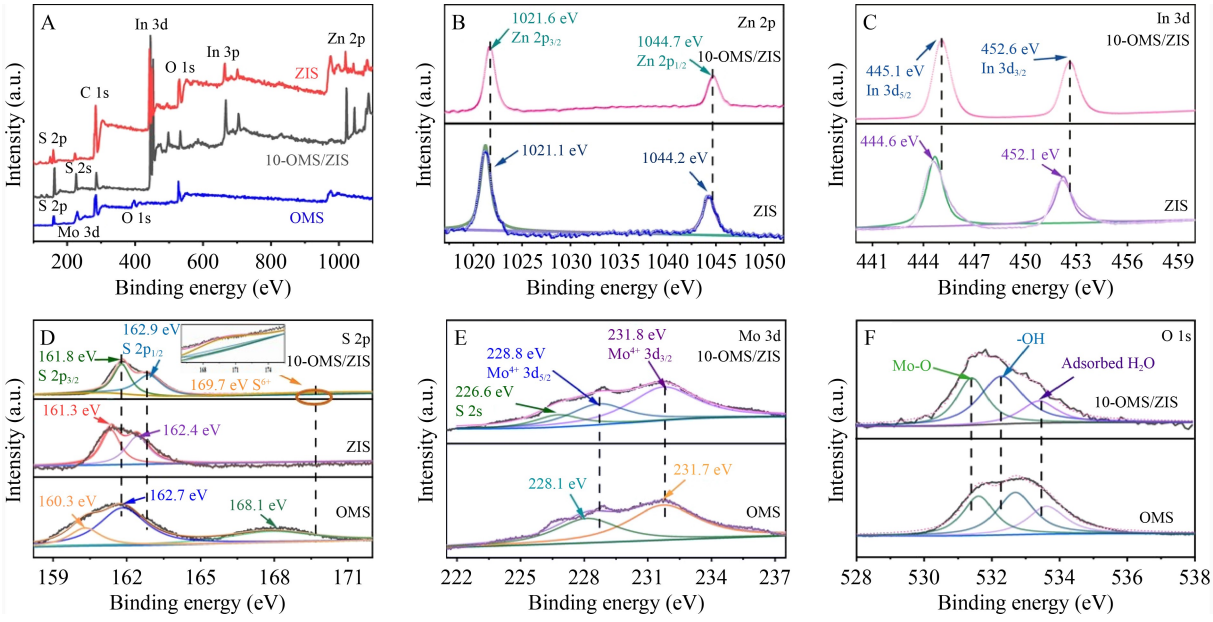


**Fig. 3** XPS spectra of (A) ZIS, OMS, and 10-OMS/ZIS; (B) Zn 2p; (C) In 3d; (D) S 2p; (E) Mo 3d; (F) O 1s.

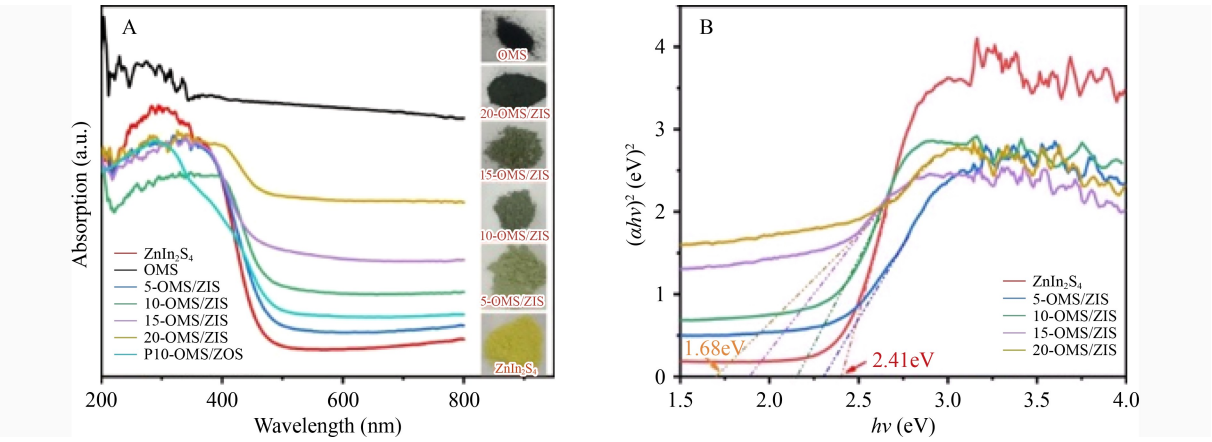


**Fig. 4** UV-vis DRS spectra of OMS, $ZnIn_2S_4$, and the OMS/ZIS composites (A), plots of $(\alpha h\nu)^2$ vs. $h\nu$ for the band gap energies of $ZnIn_2S_4$ and the OMS/ZIS composites (B).

### 3.2 HER performance evaluation

The photocatalytic HER performance results are presented in Figs. 5(A) and 5(B), showing that $H_2$ could not be detected in the dark, and suggesting that HER was a light-driven process. Pristine $ZnIn_2S_4$ and OMS showed relatively lower HER activity due to the rapid recombination of photogenerated electron-hole pairs. However, the HER rate of the OMS/ZIS composite improved with increasing OMS content, achieving a maximum of 12.8 mmol/g/h at an OMS content of 10%, which was nearly 4.9 times higher than pristine $ZnIn_2S_4$. The 10-OMS/ZIS composite exhibited satisfactory HER activity compared to a previously reported $MoS_2$-$ZnIn_2S_4$ composite (Table S2). Nevertheless, HER performance evidently decreased with higher OMS loading. These results were likely due to the lower amounts of OMS, which led to greater separation of the electron-hole pairs and excessive amounts of OMS turned into a recombination center for the photo-induced electron hole pair. Furthermore, the apparent quantum efficiency (AQE, obtained by Eq. (S1)) at 420 nm was 14.9% (Fig. 5(C)), and the wavelength-dependent HER performance was consistent with the light absorption capacity of $ZnIn_2S_4$, but not with the 10-OMS/ZIS composite (Fig. 5(C)). This suggested that the photogenerated electrons for HER were mainly derived from $ZnIn_2S_4$, and the OMS expended electrons to catalyze $H_2$ evolution (Mo et al., 2018; Zhang et al., 2020).

The durability evaluation results of the 10-OMS/ZIS composite are shown in Fig. 5(D). HER activity showed minimal deterioration in the cycle test, which was possibly related to the consumption of sacrificial reagents (Du et al., 2019). Although the activity of $H_2$ evolution exhibited a slight decrease, it still demonstrated higher activity compared to the previously reported $MoS_2$-$ZnIn_2S_4$ composite (Table S2). The reclaimed 10-OMS/ZIS photocatalyst was also characterized by XRD and SEM. As shown in Figs. S6 and S7, no distinct differences in the physical integrity and microstructure were observed between the fresh and used samples, confirming the sufficient stability of the 10-OMS/ZIS photocatalyst.

### 3.3 Simultaneous photocatalytic HER and organic degradation performance

The results of photocatalytic hydrogen production and simultaneous organic pollutant decomposition performance are shown in Fig. 6. As presented in Figs. 6(A) and 6(B), the relationship between the initial HER rate and the initial BPA concentration was set in the range of 0 to 50 mg/L, according to the Langmuir-Hinshelwood equation (Eq. (S2)) (Li et al., 2020), Accordingly, the initial HER rate was dependent on the average HER quantity in the previous hour. A detailed analysis is provided in the Supplementary Material. Subsequently, the HER rate drastically increased when the BPA concentration was less than 50 mg/L (Fig. S8), indicating that more BPA molecules were available to react with the photoexcited holes. Then, the HER rate slightly decreased when the BPA concentration further increased. This was possibly caused by the excess adsorption of BPA, which reduced the adsorbable active sites of the H atom (Xiao et al., 2012). As shown in Figs. 6(C) and 6(D), the HER rate in distilled water was 22.4 μmol/g/h over 10-OMS/ZIS, whereas the HER rates markedly increased when BPA, RC, and TC were respectively added to the photo-reaction system. This indicated that the added organics could act as electron donors, suppressing photo-induced carrier recombination. The HER rates in the BPA, RC, and TC solutions were 672.7, 232.2, and 84.1 μmol/g/h, while the corresponding degradation rates were 53.0%, 41.5%, and 63.5%, respectively. As a result, the HER rate followed the order of BPA > RC > TC > $H_2O$, suggesting that the organic type had a significant influence on photocatalytic $H_2$ production. Interestingly, the organic degradation rate followed the order TC > BPA > RC, which was consistent with the adsorption experiment results, as displayed in Figs. 6(D) and S9. The detailed adsorption experiments were shown in Supplementary Material and the adsorption

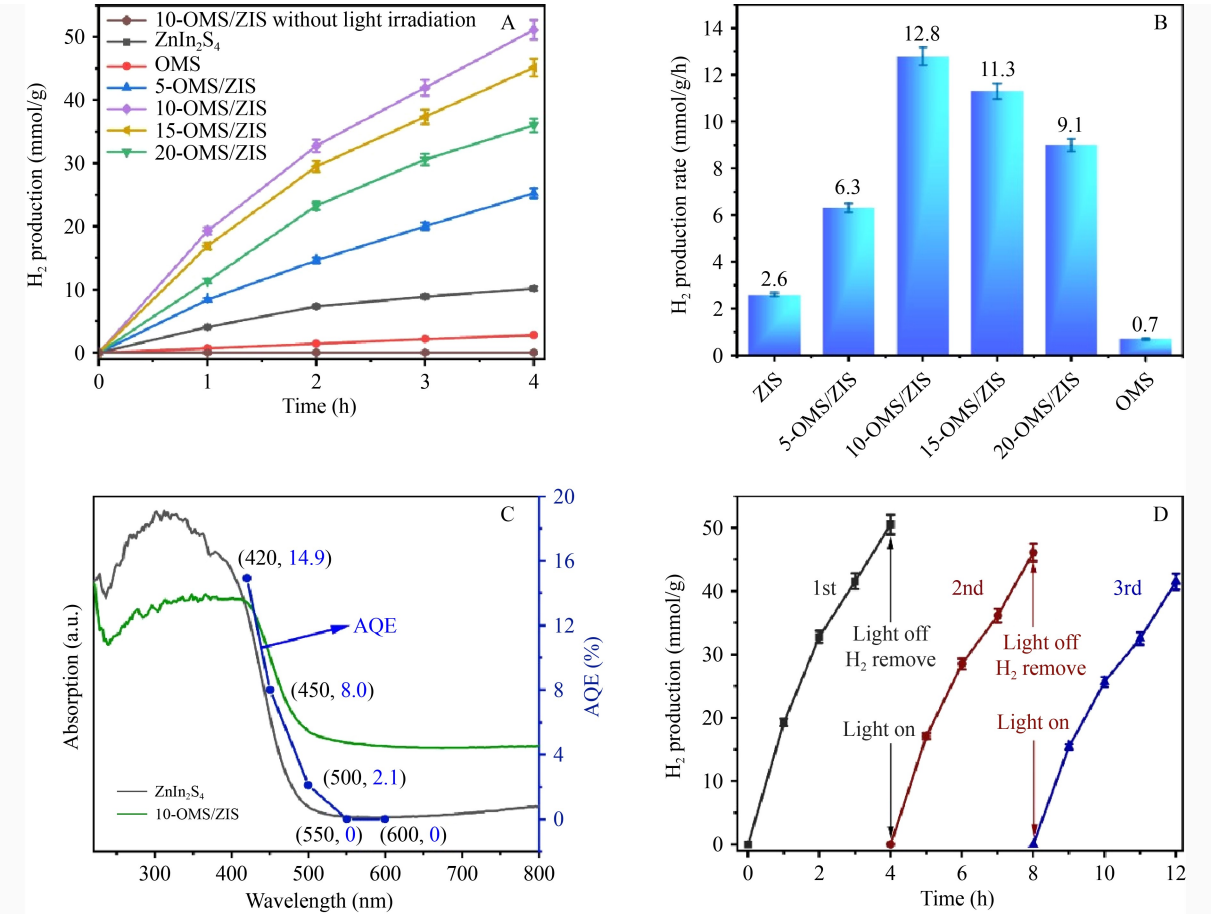


**Fig. 5** Plots of photocatalytic HER quantity vs. irradiation time (A); comparison of the HER rate for the as-synthesized samples under visible-light (B); UV-vis spectra and AQE of $ZnIn_2S_4$ and 10-OMS/ZIS (C); cycling experiment of photocatalytic HER activity over 10-OMS/ZIS (D). Error bars show the standard deviation of repeated measurements ($n$ = 3).

capacity were calculated by Eq. (S3). Additionally, the photolysis experimental results further confirmed the photochemical stability of TC, RC, and BPA (Fig. S10).

Figure 7(A) displays the dual-purpose photocatalytic performance over the 10-OMS/ZIS composite using NOM as the matrix. The high-intensity fluorescence region of actual raw water was located at excitation wavelength/emission wavelengths of 250–400 nm/380–500 nm, indicating numerous humic-like substances in the lake water (Maqbool et al., 2020). After the photocatalytic test, the peak intensity decreased significantly, implying efficient damage of the humic-like substances. The decomposition efficiency was about 54.8% after 4 h (Fig. 7(B)). Moreover, the characteristic UV-vis absorbance decreased from 0.205 to 0.088 at 254 nm, and the obtained HER rate was 237.1 μmol/g/h (Fig. 7(C)), which confirmed that NOM could be efficiently utilized as an electron donor for $H_2$ production, indicating the promising practicability of photocatalytic $H_2$ evolution and simultaneous natural water purification.

### 3.4 Charge transfer properties

The transmission and separation efficiencies of the carriers were monitored according to their steady-state photoluminescence (PL) spectra. As shown in Fig. 8(A), the 10-OMS/ZIS exhibited the lowest PL intensity, indicating that recombination of the photo-induced electron-holes was significantly suppressed, which was beneficial for improving photoactivity (Chen et al., 2018). Moreover, photogenerated carrier lifetime was recorded by the transient-state PL spectra (Fig. 8(B)). The respective kinetic parameters after bi-exponential fitting are listed in Table S3. The average decay lifetime increased from 2.84 to 4.57 ns (Eqs. (S4) and (S5)) after OMS adoption, and this extended carrier lifetime indicated that recombination of the electron-hole pairs on 10-OMS/ZIS was suppressed, which was favorable for photocatalytic HER. As shown in Fig. 8(C), the maximum photocurrent intensity of 10-OMS/ZIS was observed compared to the other samples, indicating the promoted separation of photoinduced charges. Electrochemical impedance spectroscopy was also performed to study charge transfer at the solid-liquid interface. As presented in Fig. 8(D), the OMS/ZIS composite exhibited a smaller semicircle than $ZnIn_2S_4$, indicating the decreased resistance of carrier transfer after OMS adoption, which was beneficial for the transmission

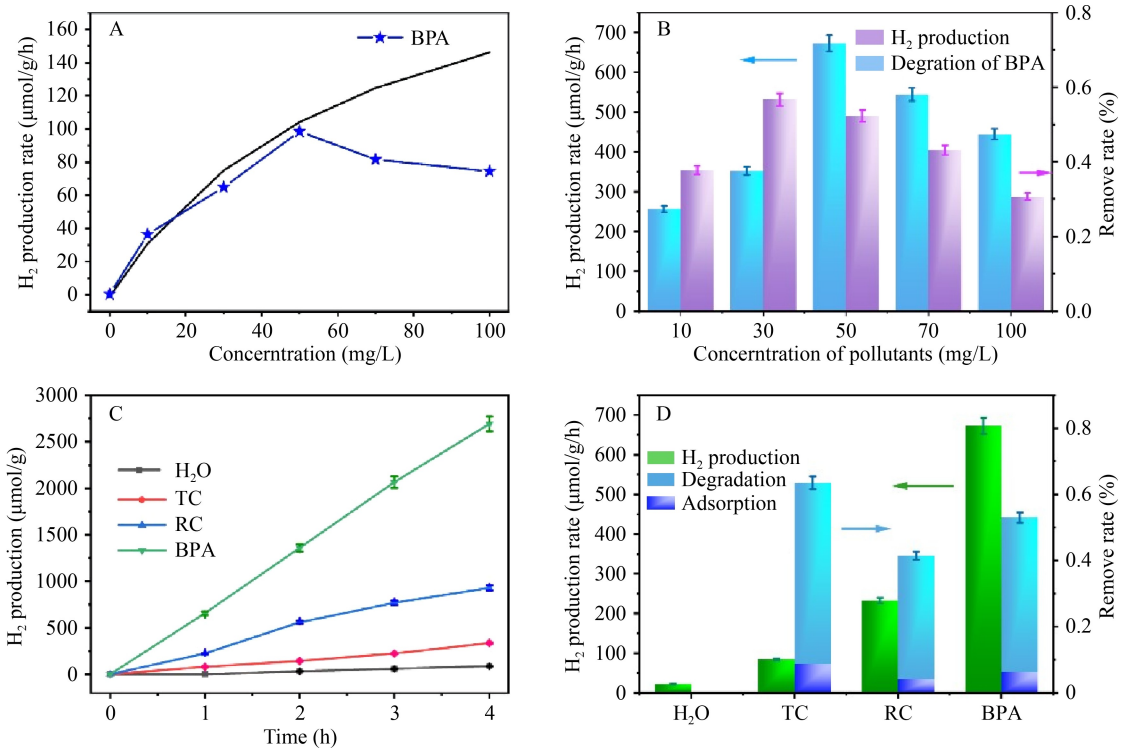


**Fig. 6** Dependence between the HER rate and BPA concentration using 10-OMS/ZIS as the photocatalyst (A), where the black line indicates Langmuir–Hinshelwood fitting; HER and simultaneous BPA degradation over 10-OMS/ZIS under visible light for 4 h at different initial concentrations (B); accumulation of $H_2$ for 4 h over different pollutants (C); simultaneous hydrogen production with pollutant degradation (D). Error bars show the standard deviation of repeated measurements ($n$ = 3).

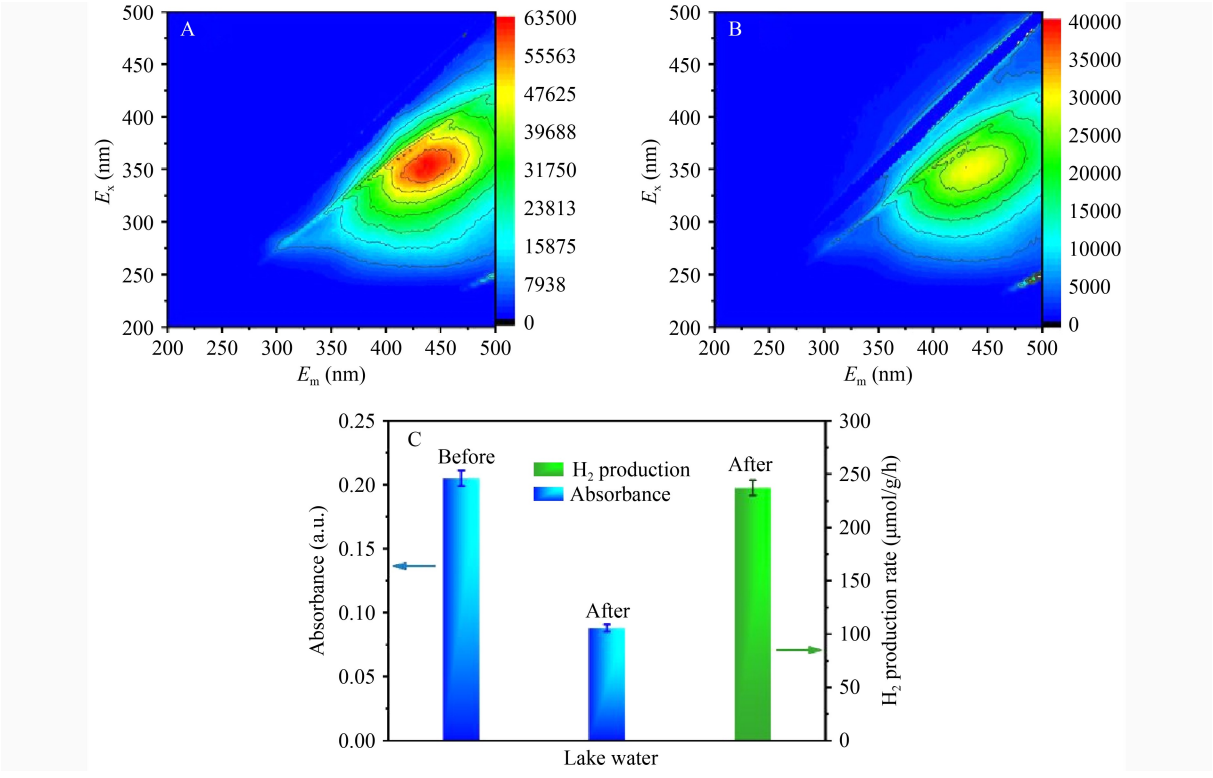


**Fig. 7** 3D EEM spectra of lake water under photocatalytic treatment: untreated (A) and after 4 h of treatment (B); UV-vis absorbance of lake water at 254 nm and the HER rate (C). Error bars show the standard deviation of repeated measurements ($n$ = 3).

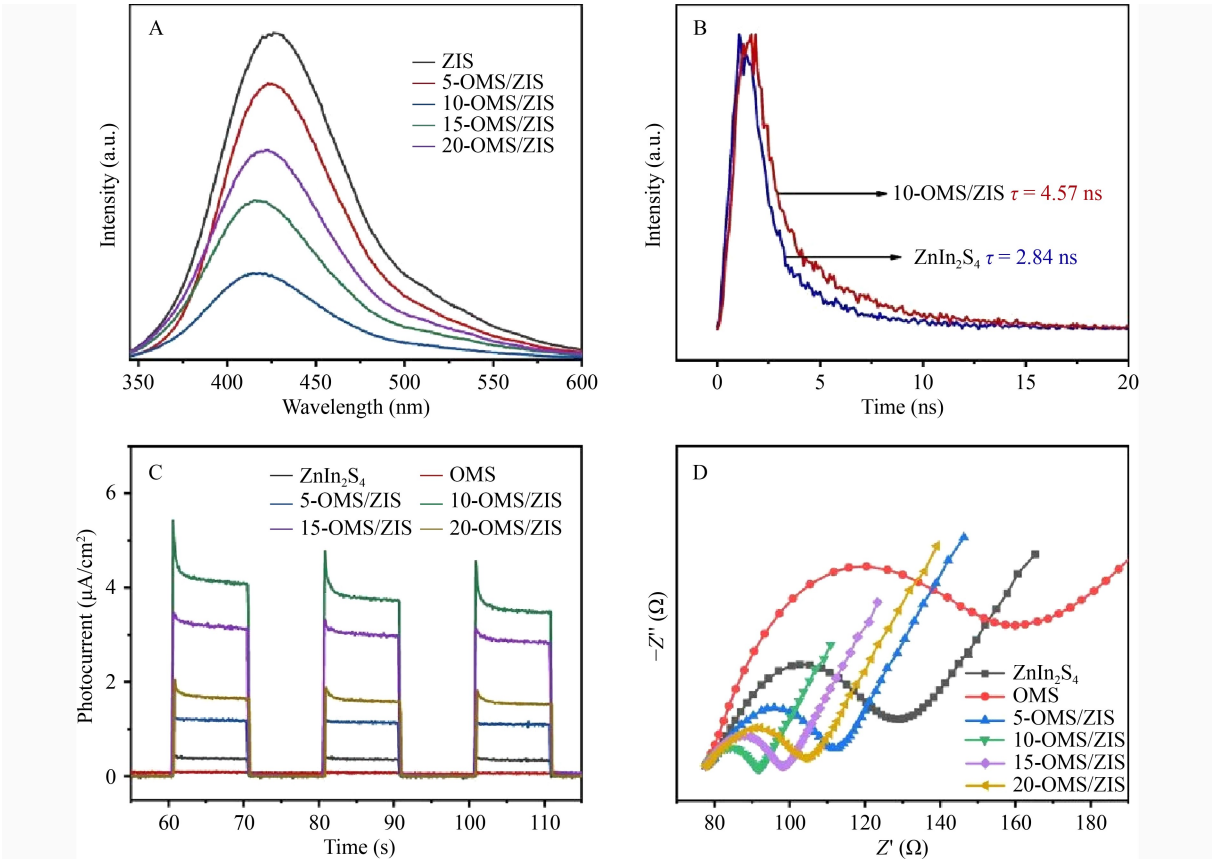


**Fig. 8** PL spectra (excitation wavelength at 335 nm in Fig. S11) (A); time-resolved fluorescence emission decay curves of $ZnIn_2S_4$ and 10-OMS/ZIS (B); transient photocurrent responses (C); EIS Nyquist plots of the as-synthesized samples (D).

of photogenerated carriers.

The electrocatalytic characteristics of $ZnIn_2S_4$ and 10-OMS/ZIS were evaluated to illustrate the effect of OMS addition on photocatalytic HER. Photoelectrochemical measurements were elaborated in Text S3. As shown in Fig. 9(A), compared to $ZnIn_2S_4$ (157 mV), the initial overpotential of HER for 10-OMS/ZIS was smaller, at approximately 71 mV. The decrease in overpotential eased the transformation from electrons to protons (Tang et al., 2016). At a current density of 10 mA/cm$^2$, the potential of 10-OMS/ZIS (243 mV) was lower than $ZnIn_2S_4$ (378 mV), indicating a stronger reductive ability. Moreover, the kinetics of charge transfer were also analyzed using the Tafel slope method. As shown in Fig. 9(B), the Tafel slopes were 116 and 209 mV/dec for 10-OMS/ZIS and $ZnIn_2S_4$, respectively, indicating that the faster electron transfer and reaction kinetics of 10-OMS/ZIS were favorable for photocatalytic HER.

### 3.5 Discussion on photoactivity improvement and organics degradation

Different organic molecules resulted in distinct HER rates in the dual-purposed photocatalytic process, which was ascribed to the synergistic effect of organic molecular structure and corresponding surface adsorption. Specifically, the organic molecules were first caught on the surface of the photocatalyst, which was the key issue for $h^+$-induced organic degradation and simultaneous effective carrier separation (Jiang et al., 2018a). As shown in Fig. 6(D), the adsorption of BPA and RC molecules on 10-OMS/ZIS was comparable, but the TC molecule (Fig. S12) showed a greater adsorption tendency on the 10-OMS/ZIS surface. These results implied that effective organic adsorption in the dual-functional system was kinetically favorable for the photocatalytic degradation reaction; thus, achieving a reasonable organic degradation efficiency. This deduction was consistent with the reports found in the literature (Sun et al., 2020). Furthermore, the lower HER rate for TC degradation was mainly attributed to the competitive adsorption of the H atoms and TC molecules that occurred on the 10-OMS/ZIS surface, resulting in a reduction of active sites for HERs (Lin et al., 2017).

Density functional theory (DFT) was used to elucidate the higher HER activity for BPA degradation compared to RC. The detailed DFT calculations were shown in Text S4. Higher HOMO energy levels typically indicate better electron donating abilities (Ma et al., 2017). As shown in Fig. 10 and Table S4, BPA showed higher HOMO energy

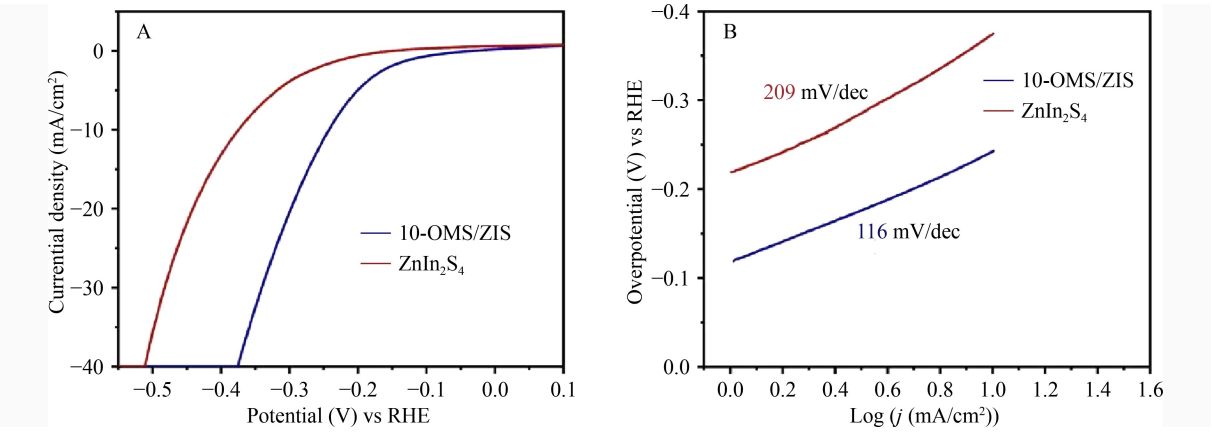


**Fig. 9** LSV curves (A) and corresponding Tafel plots of $ZnIn_2S_4$ and 10-OMS/ZIS (B).

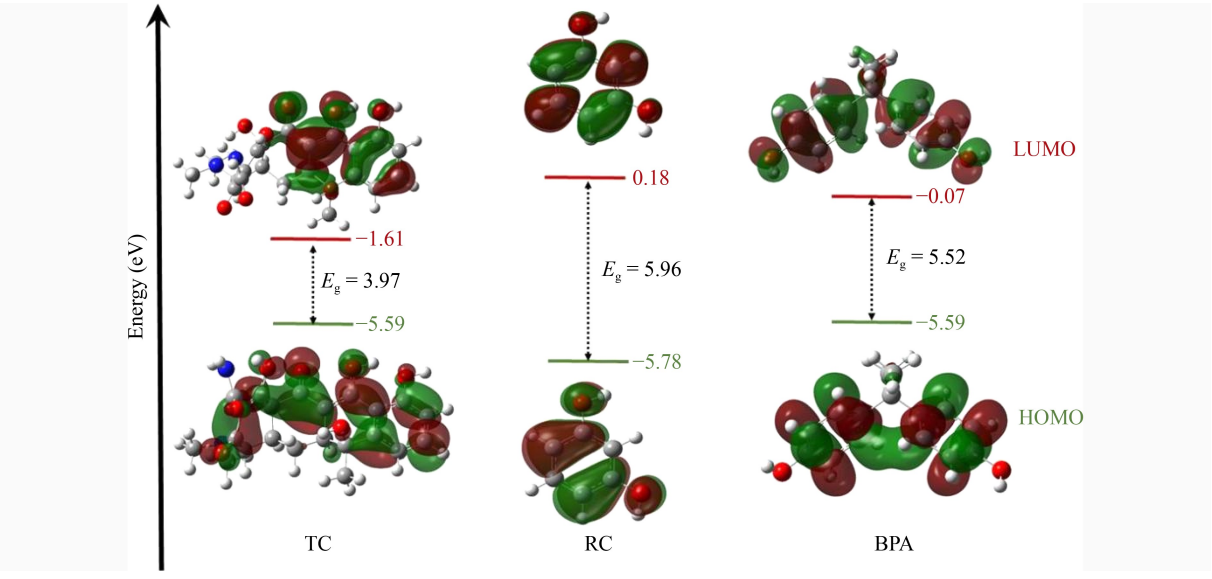


**Fig. 10** Frontier electron densities of LUMO and HOMO for TC, RC, and BPA.

levels than RC, inferring that the BPA molecule was more vulnerable to destruction by the photo-generated $h^+$ to a certain extent, resulting in more efficient separation of the electron-hole pairs and a higher HER rate.

### 3.6 Photocatalytic mechanisms

Trapping experiments with quenchers were performed to further elucidate the inherent mechanism of photocatalytic $H_2$ evolution and simultaneous organic degradation. As shown in Fig. S13, the addition of triethanolamine distinctly inhibited the degradation efficiency of TC, BPA, and RC, indicating that $h^+$ was the main active species in the dual-purpose process, and that TC, BPA, and RC were mainly decomposed by the direct oxidation of $h^+$. Moreover, ·OH and $\cdot O_2^-$ had limited influence on the organic degradation reaction. Considering the valence band potentials of $ZnIn_2S_4$ (+1.70 V vs. NHE) and the redox potentials of $\cdot OH/H_2O$ (+2.68 V vs. NHE) and $O_2/\cdot O_2^-$ (−0.33 V vs. NHE), photo-induced $h^+$ from $ZnIn_2S_4$ could not directly oxidize $H_2O$ into ·OH, but could split $H_2O$ to $O_2$ in a vacuum (Wan et al., 2017). Therefore, the observed ·OH was attributed to the indirect $\cdot O_2^-$ radical reaction route, which originated from the oxygen reduction reaction by the photo-excited electrons of $ZnIn_2S_4$ (Wang et al., 2019).

The proposed mechanism of photocatalytic $H_2$ evolution and simultaneous pollutant degradation is described in Scheme 2. The urchin-like microstructure of 10-OMS/ZIS provided abundant active sites and fast charge transfer channels, which further shortened the charge migration distance, and compressed the recombination of electron-hole pairs. The extended charge carrier lifetime decreased the activation barrier and kinetically facilitated photocatalytic HER. Moreover, the matched energy band positions of $ZnIn_2S_4$ and $MoS_2$ facilitated the transmission of photo-generated carriers, and the broader light absorption range of 10-OMS/ZIS improved light utilization efficiency. Under visible light irradiation, the photo-generated electrons on the CB of $ZnIn_2S_4$ were transferred to $MoS_2$,

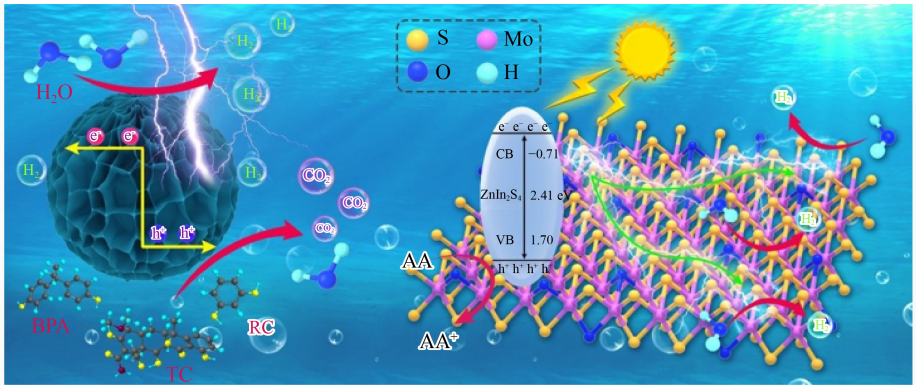


**Scheme 2** Schematic showing the possible mechanism of the OMS/ZIS composite for simultaneous photocatalytic HER and organic degradation.

which then trapped $H^+$ ions on the 10-OMS/ZIS surface, which were reduced to $H_2$ by the photo-induced electrons (Yuan et al., 2017). Because the oxidation potentials of BPA, RC, and TC (+0.454 V, +0.69 V, and +1.15 V in Fig. S14) were all smaller than the VB of $ZnIn_2S_4$ (+1.70 V in Fig. S4), the holes were consumed by the direct oxidation of organic molecules. Moreover, competitive adsorption of H atoms and organic molecules, as well as the synergistic effect between organic molecule structure and the corresponding surface adsorption had a significant influence on HER activity and organic degradation efficiency.

## 4 Conclusions

In this study, an urchin-like OMS/ZIS composite with a considerably higher and stable photocatalytic $H_2$ evolution activity was assembled for the first time using a simple solvothermal method. The highest efficiency was obtained over 10-OMS/ZIS with an HER rate of 12.8 mmol/g/h under visible light conditions. The excellent photocatalytic $H_2$ evolution activity was ascribed to the unique micro-structure, which contained abundant active sites and fast charge transfer channels and shortened the charge migration distance and compressed the carrier recombination. This resulted in a reduction in the charge transfer resistance and lower overpotential of HER. Furthermore, the results of photocatalytic $H_2$ evolution over different organic molecules illustrated the outstanding photocatalytic dual-purpose performance, in which HER was driven by the photo-induced electrons and the organics were mainly decomposed by the holes through direct oxidation. The distinct HER rate differences using different organic molecules as electron donors were likely due to the synergistic effect between the organic molecule structure and corresponding adsorption on the photocatalyst surface. This study may provide new insights into the design of high-activity dual-functional photocatalysts for environmental and energy applications.

**Acknowledgements** This study was supported by the National Key Scientific Instrument and Equipment Development Project of China (No. 21627809), the National Natural Science Foundation of China (No. 21777056), the Natural Science Foundation of Shandong Province (China) (Nos. ZR2020MB091 and ZR2020MB037), the Youth Innovative Talents Recruitment and Cultivation Program of Shandong Higher Education (China), and the Jinan Scientific Research Leader Workshop Project (China) (No. 2018GXRC021).

**Electronic Supplementary Material** Supplementary material is available in the online version of this article at https://doi.org/10.1007/s11783-022-1566-z and is accessible for authorized users.

## References

Byskov L S, Nørskov J K, Clausen B S, Topsøe H (1999). DFT calculations of unpromoted and promoted $MoS_2$-based hydrodesulfurization catalysts. Journal of Catalysis, 187(1): 109–122

Chai B, Liu C, Wang C, Yan J, Ren Z (2017). Photocatalytic hydrogen evolution activity over $MoS_2/ZnIn_2S_4$ microspheres. Chinese Journal of Catalysis, 38(12): 2067–2075

Chandrasekaran S, Yao L, Deng L, Bowen C, Zhang Y, Chen S, Lin Z, Peng F, Zhang P (2019). Recent advances in metal sulfides: from controlled fabrication to electrocatalytic, photocatalytic and photoelectrochemical water splitting and beyond. Chemical Society Reviews, 48(15): 4178–4280

Chen G, Ding N, Li F, Fan Y, Luo Y, Li D, Meng Q (2014). Enhancement of photocatalytic $H_2$ evolution on $ZnIn_2S_4$ loaded with in-situ photo-deposited $MoS_2$ under visible light irradiation. Applied Catalysis B: Environmental, 160−161: 614−620

Chen S, Li S, Xiong L, Wang G (2018). In-situ growth of $ZnIn_2S_4$ decorated on electrospun $TiO_2$ nanofibers with enhanced visible-light photocatalytic activity. Chemical Physics Letters, 706: 68–75

Cho Y J, Moon G H, Kanazawa T, Maeda K, Choi W (2016). Selective dual-purpose photocatalysis for simultaneous $H_2$ evolution and mineralization of organic compounds enabled by a $Cr_2O_3$ barrier layer coated on $Rh/SrTiO_3$. Chemical Communications, 52(62): 9636–9639

Daskalaki V M, Antoniadou M, Li Puma G, Kondarides D I, Lianos P (2010). Solar light-responsive $Pt/CdS/TiO_2$ photocatalysts for hydrogen production and simultaneous degradation of inorganic or organic sacrificial agents in wastewater. Environmental Science &

Technology, 44(19): 7200–7205

Ding N, Fan Y, Luo Y, Li D, Meng Q (2015). Enhancement of $H_2$ evolution over new $ZnIn_2S_4$/RGO/$MoS_2$ photocatalysts under visible light. APL Materials, 3(10): 104417

Du C, Zhang Q, Lin Z, Yan B, Xia C, Yang G (2019). Half-unit-cell $ZnIn_2S_4$ monolayer with sulfur vacancies for photocatalytic hydrogen evolution. Applied Catalysis B: Environmental, 248: 193–201

Eisenstein M (2015). Pesticides: Seeking answers amid a toxic debate. Nature, 521(7552): S52–S55

Gao B, Du X, Ma Y, Li Y, Li Y, Ding S, Song Z, Xiao C (2020). 3D flower-like defected $MoS_2$ magnetron-sputtered on candle soot for enhanced hydrogen evolution reaction. Applied Catalysis B: Environmental, 263: 117750

Guan Z, Wang P, Li Q, Li G, Yang J (2018). Constructing a $ZnIn_2S_4$ nanoparticle/$MoS_2$-RGO nanosheet 0D/2D heterojunction for significantly enhanced visible-light photocatalytic $H_2$ production. Dalton Transactions (Cambridge, England), 47(19): 6800−6807

Hao M, Deng X, Xu L, Li Z (2019). Noble metal free $MoS_2$/$ZnIn_2S_4$ nanocomposite for acceptorless photocatalytic semi-dehydrogenation of 1,2,3,4-tetrahydroisoquinoline to produce 3,4-dihydroisoquinoline. Applied Catalysis B: Environmental, 252: 18–23

Hou Y, Laursen A B, Zhang J, Zhang G, Zhu Y, Wang X, Dahl S, Chorkendorff I (2013). Layered nanojunctions for hydrogen-evolution catalysis. Angewandte Chemie International Edition, 52(13): 3621–3625

Hu P, Su H, Chen Z, Yu C, Li Q, Zhou B, Alvarez P J J, Long M (2017). Selective degradation of organic pollutants using an efficient metal-free catalyst derived from carbonized polypyrrole via peroxy-monosulfate activation. Environmental Science & Technology, 51(19): 11288–11296

Huang T, Chen W, Liu T Y, Hao Q L, Liu X H (2017). $ZnIn_2S_4$ hybrid with $MoS_2$: A non-noble metal photocatalyst with efficient photocatalytic activity for hydrogen evolution. Powder Technology, 315: 157–162

Jiang G, Wang K, Li J, Fu W, Zhang Z, Johnson G, Lv X, Zhang Y, Zhang S, Dong F (2018a). Electrocatalytic hydrodechlorination of 2,4-dichlorophenol over palladium nanoparticles and its pH-mediated tug-of-war with hydrogen evolution. Chemical Engineering Journal, 348: 26–34

Jiang X H, Wang L C, Yu F, Nie Y C, Xing Q J, Liu X, Pei Y, Zou J P, Dai W L (2018b). Photodegradation of organic pollutants coupled with simultaneous photocatalytic evolution of hydrogen using quantum-dot-modified g-$C_3N_4$ catalysts under visible-light irradiation. ACS Sustainable Chemistry & Engineering, 6(10): 12695–12705

Jo W K, Natarajan T S (2016). Fabrication and efficient visible light photocatalytic properties of novel zinc indium sulfide ($ZnIn_2S_4$) - graphitic carbon nitride (g-$C_3N_4$)/bismuth vanadate ($BiVO_4$) nanorod-based ternary nanocomposites with enhanced charge separation via Z-scheme transfer. Journal of Colloid and Interface Science, 482: 58–72

Kampouri S, Nguyen T N, Spodaryk M, Palgrave R G, Züttel A, Smit B, Stylianou K C (2018). Concurrent photocatalytic hydrogen generation and dye degradation using MIL‐125‐$NH_2$ under visible light irradiation. Advanced Functional Materials, 28(52): 1806368

Kampouri S, Stylianou K C (2019). Dual-functional photocatalysis for simultaneous hydrogen production and oxidation of organic substances. ACS Catalysis, 9(5): 4247–4270

Li T, Zhong W, Jing C, Li X, Zhang T, Jiang C, Chen W (2020). Enhanced hydrolysis of p-nitrophenyl phosphate by iron (hydr) oxide nanoparticles: Roles of exposed facets. Environmental Science & Technology, 54(14): 8658–8667

Li W, Lin Z, Yang G (2017). A 2D self-assembled $MoS_2$/$ZnIn_2S_4$ heterostructure for efficient photocatalytic hydrogen evolution. Nanoscale, 9(46): 18290–18298

Li Y, Lu G, Li S (2001). Photocatalytic hydrogen generation and decomposition of oxalic acid over platinized $TiO_2$. Applied Catalysis A, General, 214(2): 179−185

Lin Z, Li L, Yu L, Li W, Yang G (2017). Dual-functional photocatalysis for hydrogen evolution from industrial wastewaters. Physical Chemistry Chemical Physics, 19(12): 8356–8362

Liu C, Wang L, Tang Y, Luo S, Liu Y, Zhang S, Zeng Y, Xu Y (2015). Vertical single or few-layer $MoS_2$ nanosheets rooting into $TiO_2$ nanofibers for highly efficient photocatalytic hydrogen evolution. Applied Catalysis B: Environmental, 164: 1–9

Liu H, Zhang J, Ao D (2018a). Construction of heterostructured $ZnIn_2S_4$@$NH_2$-MIL-125(Ti) nanocomposites for visible-light-driven $H_2$ production. Applied Catalysis B: Environmental, 221: 433–442

Liu J, Fang W, Wei Z, Qin Z, Jiang Z, Shangguan W (2018b). Metallic 1T-$Li_xMoS_2$ co-catalyst enhanced photocatalytic hydrogen evolution over $ZnIn_2S_4$ floriated microspheres under visible light irradiation. Catalysis Science & Technology, 8(5): 1375–1382

Liu K H, Zhong H X, Li S J, Duan Y X, Shi M M, Zhang X B, Yan J M, Jiang Q (2018c). Advanced catalysts for sustainable hydrogen generation and storage via hydrogen evolution and carbon dioxide/nitrogen reduction reactions. Progress in Materials Science, 92: 64–111

Ma J, Wang H, Liu X, Lu L, Nie L, Yang X, Chai Y, Yuan R (2017). Synthesis of tube shape MnO/Cp composite from 3,4,9,10-perylenetetracarboxylic dianhydride for lithium ion batteries. Chemical Engineering Journal, 309: 545–551

Maqbool T, Qin Y, Ly Q V, Zhang J, Li C, Asif M B, Zhang Z (2020). Exploring the relative changes in dissolved organic matter for assessing the water quality of full-scale drinking water treatment plants using a fluorescence ratio approach. Water Research, 183: 116125

Mo Z, Xu H, Chen Z, She X, Song Y, Wu J, Yan P, Xu L, Lei Y, Yuan S, Li H (2018). Self-assembled synthesis of defect-engineered graphitic carbon nitride nanotubes for efficient conversion of solar energy. Applied Catalysis B: Environmental, 225: 154–161

Nie Y C, Yu F, Wang L C, Xing Q J, Liu X, Pei Y, Zou J P, Dai W L, Li Y, Suib S L (2018). Photocatalytic degradation of organic pollutants coupled with simultaneous photocatalytic $H_2$ evolution over graphene quantum dots/Mn-N-$TiO_2$/g-$C_3N_4$ composite catalysts: performance and mechanism. Applied Catalysis B: Environmental, 227: 312–321

Patsoura A, Kondarides D I, Verykios X E (2006). Enhancement of photoinduced hydrogen production from irradiated Pt/$TiO_2$ suspensions with simultaneous degradation of azo-dyes. Applied

Catalysis B: Environmental, 64(3-4): 171–179

Sun N, Qu Y, Yang C, Yang Z, Yan R, E W, Zhang Z, Li Z, Li H, Khan I (2020). Efficiently photocatalytic degradation of monochlorophenol on in-situ fabricated $BiPO_4/\beta$-$Bi_2O_3$ heterojunction microspheres and $O_2$-free hole-induced selective dechloridation conversion with $H_2$ evolution. Applied Catalysis B: Environmental, 263: 118313

Swain G, Sultana S, Parida K (2019). One-pot-architectured Au-nanodot-promoted $MoS_2/ZnIn_2S_4$: A novel p–n heterojunction photocatalyst for enhanced hydrogen production and phenol degradation. Inorganic Chemistry, 58(15): 9941–9955

Tang Y J, Wang Y, Wang X L, Li S L, Huang W, Dong L Z, Liu C H, Li Y F, Lan Y Q (2016). Molybdenum disulfide/nitrogen-doped reduced graphene oxide nanocomposite with enlarged interlayer spacing for electrocatalytic hydrogen evolution. Advanced Energy Materials, 6(12): 1600116

Tian G, Chen Y, Ren Z, Tian C, Pan K, Zhou W, Wang J, Fu H (2014). Enhanced photocatalytic hydrogen evolution over hierarchical composites of $ZnIn_2S_4$ nanosheets grown on $MoS_2$ slices. Chemistry, An Asian Journal, 9(5): 1291−1297

Wan S, Ou M, Zhong Q, Zhang S, Song F (2017). Construction of Z-scheme photocatalytic systems using $ZnIn_2S_4$, $CoO_x$-loaded $Bi_2MoO_6$ and reduced graphene oxide electron mediator and its efficient nonsacrificial water splitting under visible light. Chemical Engineering Journal, 325: 690–699

Wang H, Wu Y, Feng M, Tu W, Xiao T, Xiong T, Ang H, Yuan X, Chew J W (2018a). Visible-light-driven removal of tetracycline antibiotics and reclamation of hydrogen energy from natural water matrices and wastewater by polymeric carbon nitride foam. Water Research, 144: 215–225

Wang Q, Huang J, Sun H, Ng Y H, Zhang K Q, Lai Y (2018b). $MoS_2$ quantum dots@$TiO_2$ nanotube arrays: An extended-spectrum-driven photocatalyst for solar hydrogen evolution. ChemSusChem, 11(10): 1708–1721

Wang S, Zhu B, Liu M, Zhang L, Yu J, Zhou M (2019). Direct Z-scheme ZnO/CdS hierarchical photocatalyst for enhanced photocatalytic $H_2$-production activity. Applied Catalysis B: Environmental, 243: 19–26

Wei L, Chen Y, Lin Y, Wu H, Yuan R, Li Z (2014). $MoS_2$ as non-noble-metal co-catalyst for photocatalytic hydrogen evolution over hexagonal $ZnIn_2S_4$ under visible light irradiations. Applied Catalysis B: Environmental, 144: 521–527

Wei Z, Liu J, Fang W, Xu M, Qin Z, Jiang Z, Shangguan W (2019). Photocatalytic hydrogen evolution with simultaneous antibiotic wastewater degradation via the visible-light-responsive bismuth spheres-g-$C_3N_4$ nanohybrid: Waste to energy insight. Chemical Engineering Journal, 358: 944–954

Wu Z, Liu X, Liu J, Liu S, Zha Z, Chen Z (2019). Molybdenum disulfide based composites and their photocatalytic degradation and hydrogen evolution properties. Progress in Chemistry, 31(8): 1086−1102 (in Chinese)

Xiao X, Hao R, Liang M, Zuo X, Nan J, Li L, Zhang W (2012). One-pot solvothermal synthesis of three-dimensional (3D) BiOI/BiOCl composites with enhanced visible-light photocatalytic activities for the degradation of bisphenol-A. Journal of Hazardous Materials, 233–234: 122–130

Xu Y, Yan A, Jiang L, Huang F, Hu D, Duan G, Zheng F (2022). $MoS_2$/HCSs/$ZnIn_2S_4$ nanocomposites with enhanced charge transport and photocatalytic hydrogen evolution performance. Journal of Alloys and Compounds, 895: 162504

Yang G, Ding H, Chen D, Feng J, Hao Q, Zhu Y (2018). Construction of urchin-like $ZnIn_2S_4$-Au-$TiO_2$ heterostructure with enhanced activity for photocatalytic hydrogen evolution. Applied Catalysis B: Environmental, 234: 260–267

Yi H, Huang D, Qin L, Zeng G, Lai C, Cheng M, Ye S, Song B, Ren X, Guo X (2018). Selective prepared carbon nanomaterials for advanced photocatalytic application in environmental pollutant treatment and hydrogen production. Applied Catalysis B: Environmental, 239: 408–424

Yuan Y J, Chen D, Zhong J, Yang L X, Wang J, Liu M J, Tu W G, Yu Z T, Zou Z G (2017). Interface engineering of a noble-metal-free 2D–2D $MoS_2$/Cu-$ZnIn_2S_4$ photocatalyst for enhanced photocatalytic $H_2$ production. Journal of Materials Chemistry. A, Materials for Energy and Sustainability, 5(30): 15771–15779

Yuan Y J, Tu J R, Ye Z J, Chen D Q, Hu B, Huang Y W, Chen T T, Cao D P, Yu Z T, Zou Z G (2016). $MoS_2$-graphene/$ZnIn_2S_4$ hierarchical microarchitectures with an electron transport bridge between light-harvesting semiconductor and cocatalyst: A highly efficient photocatalyst for solar hydrogen generation. Applied Catalysis B: Environmental, 188: 13–22

Zhang G, Chen D, Li N, Xu Q, Li H, He J, Lu J (2020). Construction of hierarchical hollow $Co_9S_8/ZnIn_2S_4$ tubular heterostructures for highly efficient solar energy conversion and environmental remediation. Angewandte Chemie, 132(21): 8332–8338

Zhang S, Gu P, Ma R, Luo C, Wen T, Zhao G, Cheng W, Wang X (2019). Recent developments in fabrication and structure regulation of visible-light-driven g-$C_3N_4$-based photocatalysts towards water purification: A critical review. Catalysis Today, 335: 65–77

Zhang S, Liu X, Liu C, Luo S, Wang L, Cai T, Zeng Y, Yuan J, Dong W, Pei Y, Liu Y (2018a). $MoS_2$ quantum dot growth induced by S vacancies in a $ZnIn_2S_4$ monolayer: atomic-level heterostructure for photocatalytic hydrogen production. ACS Nano, 12(1): 751–758

Zhang S, Wang L, Liu C, Luo J, Crittenden J, Liu X, Cai T, Yuan J, Pei Y, Liu Y (2017). Photocatalytic wastewater purification with simultaneous hydrogen production using $MoS_2$ QD-decorated hierarchical assembly of $ZnIn_2S_4$ on reduced graphene oxide photocatalyst. Water Research, 121: 11–19

Zhang X H, Li N, Wu J, Zheng Y Z, Tao X (2018b). Defect-rich O-incorporated 1T-$MoS_2$ nanosheets for remarkably enhanced visible-light photocatalytic $H_2$ evolution over CdS: The impact of enriched defects. Applied Catalysis B: Environmental, 229: 227–236

Zhang Z, Huang L, Zhang J, Wang F, Xie Y, Shang X, Gu Y, Zhao H, Wang X (2018c). *In situ* constructing interfacial contact $MoS_2/ZnIn_2S_4$ heterostructure for enhancing solar photocatalytic hydrogen evolution. Applied Catalysis B: Environmental, 233: 112–119

Zhao T, Xing Z, Xiu Z, Li Z, Yang S, Zhou W (2019). Oxygen-doped $MoS_2$ nanospheres/CdS quantum dots/g-$C_3N_4$ nanosheets super-architectures for prolonged charge lifetime and enhanced visible-light-driven photocatalytic performance. ACS Applied Materials & Interfaces, 11(7): 7104–7111